Title

Engineering the Cellular Microenvironment: Integrating Three-Dimensional Nontopographical and Two-Dimensional Biochemical Cues for Precise Control of Cellular Behavior.

Journal

ACS Nano, 18(29)

Authors

Sarikhani, Einollah

Meganathan, Dhivya

Larsen, Anne-Kathrine

et al.

Publication Date

2024-07-23

DOI

10.1021/acsnano.4c03743

Peer reviewed

ACS NANO

www.acsnano.org

ARTICLE

Engineering the Cellular Microenvironment: Integrating Three-Dimensional Nontopographical and Two-Dimensional Biochemical Cues for Precise Control of Cellular Behavior

Einollah Sarikhani, Dhivya Pushpa Meganathan, Anne-Kathrine Kure Larsen, Keivan Rahmani, Ching-Ting Tsai, Chih-Hao Lu, Abel Marquez-Serrano, Leah Sadr, Xiao Li, Mingdong Dong, Francesca Santoro, Bianxiao Cui, Lasse Hyldgaard Klausen,* and Zeinab Jahed*

Cite This: *ACS Nano* 2024, 18, 19064–19076

Read Online

ACCESS | Metrics & More | Article Recommendations | Supporting Information

ABSTRACT: **The development of biomaterials capable of regulating cellular processes and guiding cell fate decisions has broad implications in tissue engineering, regenerative medicine, and cell-based assays for drug development and disease modeling. Recent studies have shown that three-dimensional (3D) nanoscale physical cues such as nanotopography can modulate various cellular processes like adhesion and endocytosis by inducing nanoscale curvature on the plasma and nuclear membranes. Two-dimensional (2D) biochemical cues such as protein micropatterns can also regulate cell function and fate by controlling cellular geometries. Development of biomaterials with precise control over nanoscale physical and biochemical cues can significantly influence programming cell function and fate. In this study, we utilized a laser-assisted micropatterning technique to manipulate the 2D architectures of cells on 3D nanopillar platforms. We performed a comprehensive analysis of cellular and nuclear morphology and deformation on both nanopillar and flat substrates. Our findings demonstrate the precise engineering of single cell architectures through 2D micropatterning on nanopillar platforms. We show that the coupling between the nuclear and cell shape is disrupted on nanopillar surfaces compared to flat surfaces. Furthermore, our results suggest that cell elongation on nanopillars enhances nanopillar-induced endocytosis. We believe our platform serves as a versatile tool for further explorations into programming cell function and fate through combined physical cues that create nanoscale curvature on cell membranes and biochemical cues that control the geometry of the cell.**

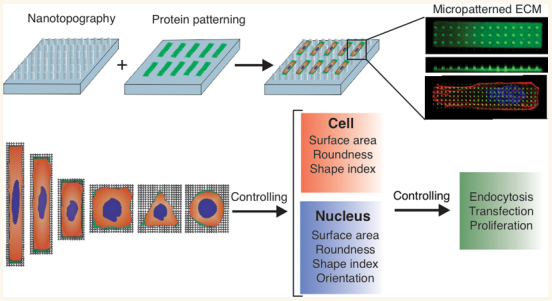

KEYWORDS: *micropatterning, cell and nuclear morphology, nanostructures, nanopillar, cell and nuclear deformation, cell and nuclear mechanics, mechanobiology*

INTRODUCTION

In recent years, the development of advanced biomaterials capable of regulating cellular processes and guiding cell fate decisions has received significant attention, especially for applications in tissue engineering,[1] regenerative medicine,[2,3] and cell-based assays.[4,5] Many studies have shown that a variety of external physical and biochemical cues can dictate cell function and fate through distinct mechanisms. For instance, 3D nanoscale physical cues on nanomaterials (nanotopography) can modulate cell function and fate by creating a nanoscale curvature on plasma and nuclear membranes. This curvature attracts specific proteins to the cell/nanomaterial interface, triggering downstream processes that influence cell signaling and behavior.[6] Instead, 2D microscale biochemical cues, such as protein micropatterns, regulate cell fate by promoting selective cell adhesion to

Received: March 19, 2024
Revised: June 13, 2024
Accepted: June 14, 2024
Published: July 9, 2024

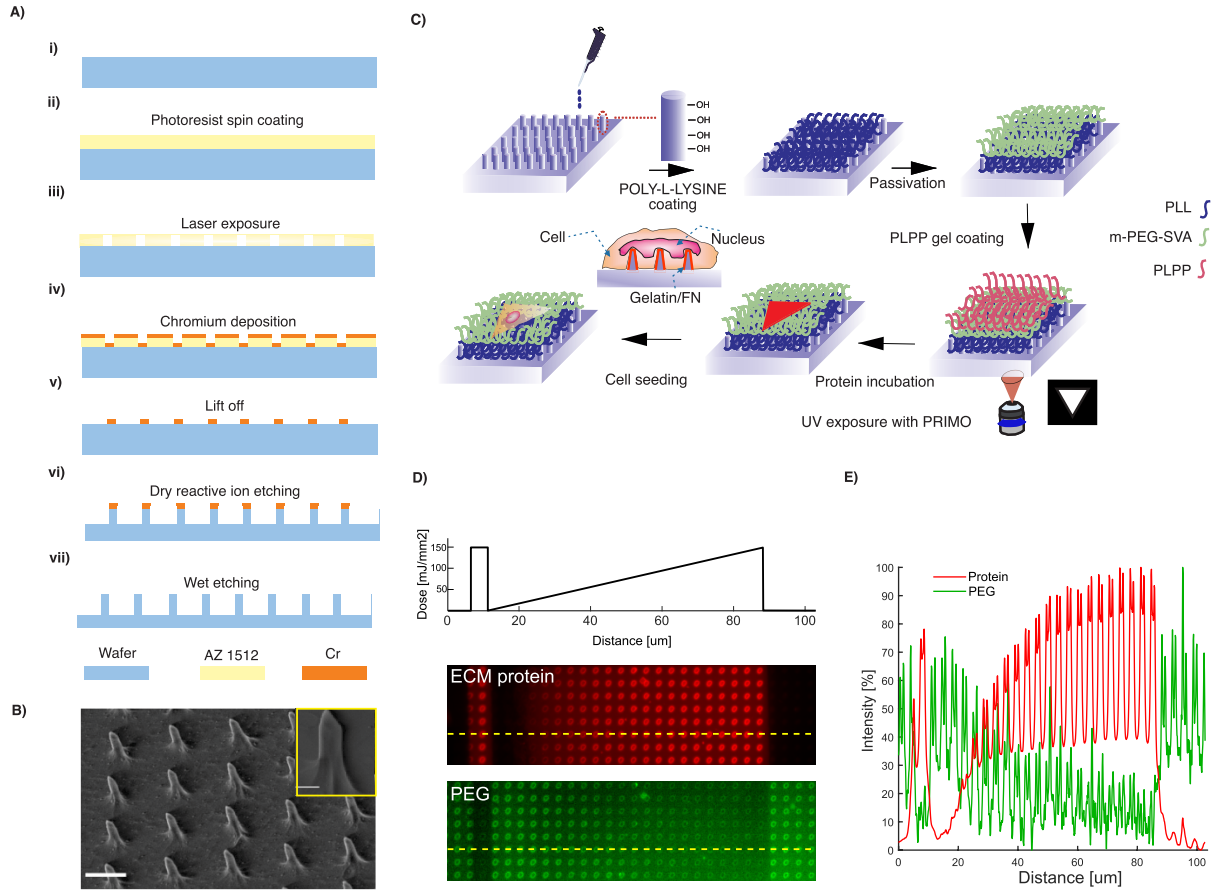

Figure 1. Engineering a controllable ECM protein patterned for studying cellular behavior on nanopillars. (A) Overview schematic of the nanopillars fabrication process including photolithography, electron beam evaporation, dry etching, and wet etching. (B) SEM image (45°) of nanopillar arrays with 1.51 ± 0.19 μm height, 0.41 ± 0.09 μm diameter, and 3.22 ± 0.43 pitch (scale bar = 5 μm). The inset shows an enlarged image of single pillar representing the size and shape of pillars (scale bar = 1 μm). (C) Schematic of protein photopatterning on the nanopillars with PRIMO system. (D) Gradient of UV exposure on PLL−PEG-FITC coated nanopillars. (E) Profile of protein and PEG intensity along yellow line in panel (D).

patterned proteins, thus imposing specific 2D protein cues that shape cell morphology. Biomaterials with combined biochemical and physical cues can significantly expand the potential for programming cell fates in various biomedical applications.

Here, we present a platform with nanoscale topography that combines biochemical and physical cues for regulating cell processes. Biomaterials with nanoscale topography have become increasingly attractive for regulating cell processes for a wide range of application in areas such as tissue engineering,[7−9] drug delivery, discovery, and development,[10−12] biosensing,[13−15] electrophysiology,[16] as well as fundamental cell biology, biophysics, and mechanobiology.[17−19] One type of nanotopographies that has gained significant attention is repeating patterns of free-standing cylinders with diameters of few hundred nanometers commonly known as nanopillar arrays.[20] Several studies have shown that cells on nanopillars display behaviors distinct from those on flat surfaces affecting crucial cellular processes including endocytosis,[21−23] adhesion,[24] proliferation,[25,26] migration,[25,26] and differentiation.[27−29] These findings have propelled the development of advanced applications by leveraging nanopillar-induced changes in cellular processes. For example, enhancement of endocytosis events on nanopillars has led to their use in platforms for highly efficient delivery of a variety of biomolecules to the cell.[30−32][21,22]

Furthermore, because of the specific properties of nanopillars such as high surface area-to-volume ratio, biocompatibility, controllability of their geometry and material, and the availability of several techniques for their high-throughput fabrication, nanopillar platforms are promising for regulating cell function.[33,34]

Recent studies have highlighted that nanopillars also influence key biophysical properties of cells and nuclei, such as shape, orientation, and spreading area.[21] The cell shape and the distribution of organelles are crucial for cellular function and fate, and these aspects vary significantly among different cell types.[35] Therefore, if nanotopography is to be effectively used as a cue to manipulate the nanoscale curvature of plasma and nuclear membranes to control cell function and fate, it is essential to achieve precise control over cell shape, spreading area, and organelle distribution on nanotopography. This level of control is important for employing the full potential of nanotopography in directing behaviors of diverse cell types.[36,37] Previous studies have attempted to control the cellular morphology, polarization, and alignment by tuning the nanopillar geometry. However, relying solely on nanotopography provides limited spatial control over the shapes of cells and organelles and the effectiveness varies by cell type.[54,55] Our method addresses these limitations by employing a maskless micropatterning technique that precisely patterns extracellular

https://doi.org/10.1021/acsnano.4c03743
ACS Nano 2024, 18, 19064−19076

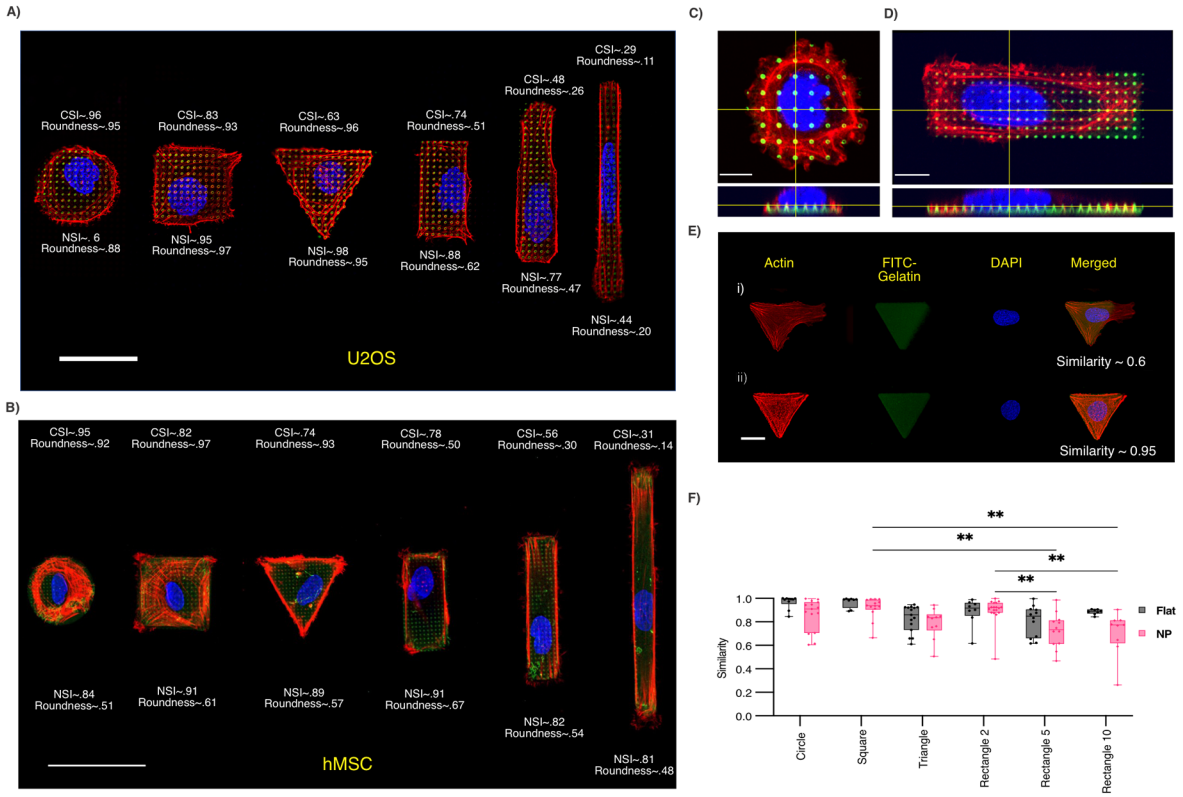

Figure 2. Engineering cell morphology on the nanopillar shapes with micropatterning technique. (A) Representative widefield image of U2OS cells on patterned proteins on nanopillars showing conformation of cells to the ECM matrix. (Scale bar = 40 μm). (B) Representative widefield image of hMSC cells on patterned proteins on nanopillars. ECM protein gelatin (green), actin (red), and nucleus (blue) are shown. (Scale bar = 50 μm). (C) Representative confocal image of U2OS cell on circular micropatterned ECM protein on nanopillars from top and side view. (Scale bar = 10 μm). (D) Representative confocal image of U2OS cell on rectangular micropatterned ECM protein on nanopillars from top and side view. (Scale bar = 10 μm). (E) Representative images of U2OS cells conforming to the ECM protein with different similarity index: (i) the cell with lower similarity to the micropatterned ECM ~ 0.6 and (ii) high similarity of the cell to the ECM ~ 0.95. ECM protein gelatin (green), actin (red), and nucleus (blue) are shown. (F) Similarity analysis of the cells conforming to the shape of the ECM proteins patterned on flat and nanopillar substrate. (Scale bar = 20 μm). (p < 0.01).**

matrix proteins (ECM) onto nanotopographies with high spatial control.

Micropatterning techniques allow precise control over cellular shape and organelle distribution of adherent cell types.[38] These techniques involve the creation of specific patterns of extracellular matrix (ECM) proteins on smooth surfaces to control single cell geometries. The size and shape of the micropatterns can significantly influence cellular processes and behaviors such as migration[39] differentiation[40] and proliferation[41] making protein patterning a key technique in biomedical applications. Micropatterning has been successfully applied across a diverse range of cell types. In stem cells, this technique has been very successful in directing differentiation toward specific lineages, such as osteoblasts for bone tissue engineering or neurons for neural tissue repair.[42−44] Micropatterns have been used to enhance the maturation and alignment of patient-derived cardiomyocytes, critical for developing cardiac tissue models and understanding heart disease mechanisms.[45] Epithelial cells have been controlled in terms of morphology and polarization through micropatterning, aiding research in barrier functions, organ morphogenesis, and cancer progression.[46−48] Micropatterns have also been used to guide the growth and network formation of neurons to investigate neural development, neurodegenerative conditions, and the creation of neural interfaces.[49,50] These examples highlight the power of protein micropatterning in providing controlled environments for guiding cell processes for diverse cell types.[51−53]

Here, we present a contact-free micropatterning technique designed to precisely engineer cellular morphologies on nanopillar arrays. This technique allows for exact control of cell and nuclear shapes across different cell types, enables single-cell resolution, and facilitates the controlled spatial organization of cells and their organelles on nanotopography. This advancement will ultimately enable the leveraging of combined effects of nanotopography-induced and cell-shape-induced control of cellular behavior to strategically program cell function and fate by highly detailed and engineered microenvironments.

RESULTS AND DISCUSSION

ECM Micropatterns on Transparent SiO_2 Nanopillar Arrays. We fabricated fused silica SiO_2 nanopillar arrays using photolithography followed by consecutive dry etching and wet etching process (Figure 1A) as detailed in the experimental section. The size and shape of the fabricated nanopillars were characterized with scanning electron microscopy as shown in Figure 1B, and the dimensions were determined (average height of 1.51 ± 0.19, diameter of 0.41 ± 0.09, and pitch of 3.22 ± 0.43 μm). The process of patterning cells on a substrate involves the use of ECM components such as fibronectin (FN), gelatin, and collagen, which facilitates binding of the

https://doi.org/10.1021/acsnano.4c03743
ACS Nano 2024, 18, 19064−19076

cells to the surface through recruitment of adhesion molecules such as integrin through the formation of focal adhesions (FA). These FA are crucial since they dictate the cellular and nuclear shape as well as cell polarity in a manner dependent on the substrate shape and polarity. For example, FA connect the substrate to the cytoskeleton by forming complexes between integrin and proteins such as vinculin (Figure S1). To pattern extracellular matrix (ECM) proteins on nanopillar arrays, we used the light-induced molecular adsorption of protein (LIMAP) technique.[56] This technique is a maskless, controllable, and noncontact patterning of protein that accommodates patterning on a variety of substrates such as glass, PDMS, and is compatible with our transparent nanopillar arrays.[57,58] To specifically attach cells to micropatterns, we coated the surface with poly-L-lysine (PLL), followed by a covalently linked layer of polyethylene glycol (PEG). Using a photoinitiator and patterned UV exposure, patterns of PEG were removed after which FITC-gelatin and fibronectin (FN) could attach to the exposed PLL (Figure 1C). To obtain the highest contrast and protein adsorption on the micropatterned areas, we optimized the dose of UV illumination by testing UV doses of 30, 90, and 240 mJ/mm^2 and obtained the optimized results at 240 mJ/mm^2, which demonstrated the highest fluorescent intensity compared to the others (Figure S2) and could produce high quality patterns of different geometrical shapes on nanopillars (Figure S3). In addition, the fluorescent intensity profile of the protein across a line showed the highest intensity on micropatterned areas and relatively low background intensity between micropatterns. This is essential for promoting specific cell attachment only in micropatterned areas. Furthermore, ECM proteins attached even at the concave base of nanopillars, which is inaccessible to standard microcontact printing (Figure S4). In fact, microcontact printing would leave the sides and immediate vicinity of nanopillars bare of protein, while the maskless photolithography approach yielded a uniform coating.

An antifouling layer of PEG was used to ensure cell attachment only on patterned areas. PEG is generally considered biologically inert, but any PEG molecules left after UV cleavage could affect cellular adhesion to nanopillars. To study the fate of PEG during UV cleavage, we fabricated a PLL−PEG-FITC surface coating and monitored the release of PEG-FITC during patterning (Figure 1D,E). Increasing UV exposure led to increasing PEG cleavage, while a slightly larger UV dose was required to ensure complete removal of PEG on nanopillars than on a flat substrate. Furthermore, the density of attached ECM protein was proportional to the amount of removed PEG. These results verified that the nanopillars were coated with a uniform layer of ECM protein, and using this technique, we robustly and reproducibly patterned hundreds of ECM shapes on nanopillars.

Different Cell Types Conform to Micropatterns of Various Shapes on Nanopillars. Having established a robust method for developing gelatin/FN micropatterns on nanopillars, we set out to control the cellular morphologies on nanopillars by confining single cells to each micropattern. To this end, we tested a variety of cell densities and found an optimal cell seeding density of 15,000 cells/cm^2 to obtain the highest number of single cells on micropatterns. We first seeded the cells on nanopillars and flat surfaces with uniform protein coating to identify the range of expected cell area (Figure S5). This furthermore illustrates the randomized morphology observed in cells in general.

We cultured cells on micropatterns with a range of shape parameters (roundness and shape index) (Figure 2A) and showed that cells conform to micropatterns of various shape parameters on nanopillar by fluorescent imaging of cell boundaries by using an actin stain (Figure 2A). To demonstrate the versatility of the current method for a variety of cell types, we seeded two cell types (Human Bone Osteosarcoma Epithelial Cells (U2OS) and Human Mesenchymal Stem Cells (hMSC)) and showed qualitatively that both conform to the shapes of micropatterns (Figure 2A,B).

To determine whether cells spread in 2D on the top of the nanopillar or wrap around nanopillars in 3D, we performed confocal fluorescence microscopy. Reconstructed side views of the cell−nanopillar interface demonstrate the cells conforming to the micropatterned area while the cell and its nucleus deform over the nanopillar arrays to engulf the nanopillars (Figure 2C,D).

Having demonstrated the versatility of our platform for two cell types, we continued experiments with U2OS cells for all statistics presented in the next sections. To demonstrate that our technique can reliably control the cell shape on nanopillars, we quantified the conformity of cells to micropattern shapes and compared it to micropatterns on flat substrates. Specifically, we calculated the similarity between cell shape and micropattern shape on both nanopillars and flat substrates. We used the FITC-gelatin/FN to determine contours of micropattern shapes and F-actin for determining cell boundaries (Figure 2E).

Additionally, we used the Hu Moments method to determine the similarity of the ECM micropattern and cell shape as detailed in the methods section.[59] The similarity values range from 0 to 1, where 1 indicates the highest value for the similarity that demonstrates the highest conformity of cell to the micropattern shape. Our results show that there are no significant differences in the similarity values for the U2OS cells on flat and nanopillar substrates for any of the micropattern shapes (Figure 2F). However, the average similarity of the cells and micropatterns and the standard deviations are slightly higher for all geometries on flat surfaces, which can be explained by the tendency of cells to grow irregularly due to the filopodia retraction membrane protrusions around the nanostructures.[18] Interestingly, although cells conform to micropatterns of any shape on flat substrates with comparable similarity values (i.e., the similarity values are not statistically different), on nanopillars, cells exhibit lower conformity to specific micropattern shapes. We observed statistically significant difference in the cell conformity to rectangular shapes with an aspect ratio of 5 and 10 compared to square shape pattens and rectangular patterns with an aspect ratio of 2, indicating that cells tend to resist elongated shapes on nanopillars, which is consistent with previous studies of cellular morphology behavior on nanostructures.[27] This analysis indicates that the micropatterning on nanopillar platform offers high controllability for a range of geometries in a single cell level. For all future experiments, we analyzed cells that conformed to the micropattern shapes with a threshold similarity value above 0.6 and excluded nonconformant cells.

Control of Cell and Nuclear Morphology on Nanopillars. To investigate the synergic effects of micropatterns and nanopillars on cellular and nuclear morphology and deformation, we compared three important shape factors: size, roundness, and shape index. A combination of these

https://doi.org/10.1021/acsnano.4c03743
ACS Nano 2024, 18, 19064−19076

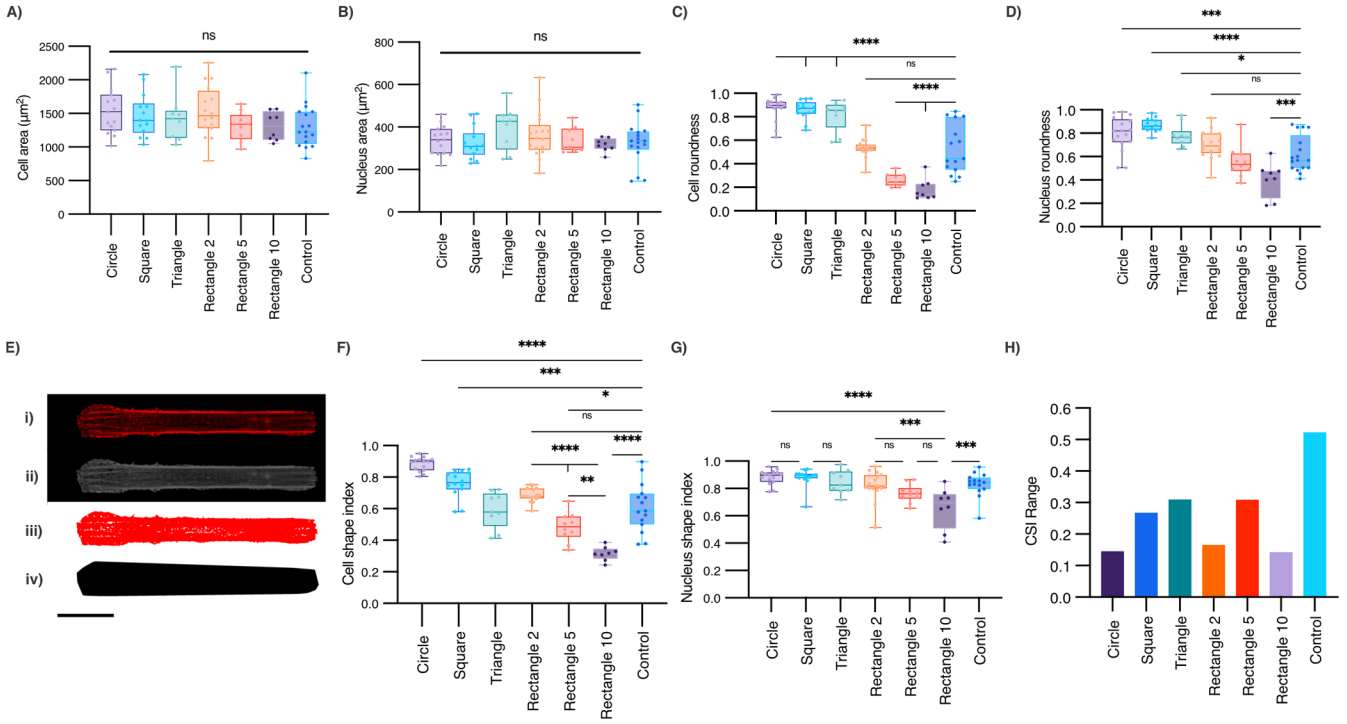

Figure 3. Morphology characteristic of U2OS cells and nucleus when grown on micropatterned nanopillars with various shapes and surface area of 1600 μm^2. Comparison of the surface area of the (A) U2OS cells and (B) nucleus grown on micropatterns. Comparison of elongation of cells based on roundness of (C) U2OS cells and (D) nucleus. (E) Imaging process of the cell shape analysis with ImageJ software: (i) images of cells stained with actin obtained, (ii) the images converted to grayscale, (iii) thresholding used to separate the cell and the background, and (iv) convex hull used to analyze the convex to analyze cell and nucleus shape index. Comparison of the (F) cell shape index (CSI) of U2OS cells and (G) nucleus cell shape index (NSI) on different micropatterns. (H) CSI spread of the cells compared with subtracting the lowest CSI from the highest CSI within each shape. ($*p < 0.05$, $**p < 0.01$, $***p < 0.001$, and $****p < 0.0001$).

parameters can provide a comprehensive understanding of the overall cell and nuclear shape in response to the external cues.

Cell and Nuclear Size. To quantify the cell and nuclear size, we measured surface area of the cell and nucleus based on actin and nucleus (DAPI) staining. Therefore, we can manipulate the shape of cells without altering their size, as our study found no significant difference in surface area among various shapes (Figure 3A). Expectedly, the nuclear surface area followed a similar trend as the cell surface area (Figure 3B). The consistency across different shapes suggests that the cells' and nuclei's intrinsic properties remain unchanged by the micropatterning, maintaining the physiological relevance of the experiment.

Cell and Nuclear Roundness. Next, we characterized the cell roundness and elongation, as a parameter that is critical to electrical and mechanical characteristics of cells such as heart and neuronal cells.[60] For example, Kim et al. studied the relationship of cell morphology on action potential and cell−cell interactions of heart muscle cells.[61] Hence, we performed a roundness analysis of the cell and nucleus on micropatterns. Roundness is defined as the ratio of the minor axis to the major axis of the cell. For instance, a perfect circle, triangle, and square have roundness equal to 1 while rectangle 2, rectangle 5, and rectangle 10 have roundness values equal to 0.5, 0.25, and 0.1, respectively. We observed that the roundness of cells varies significantly on different geometries of ECM protein patterns. While the cells had obvious variation in roundness when spread on other shapes, rectangular shape with an aspect ratio of 2 had the highest similarity to the control cells (nonpatterned) (Figure 3C). The nuclear deformation on micropatterns also exhibited a trend similar to the cellular response, with the rectangular shapes with aspect ratios of 2 and 5 having no significant difference from the control cells (Figure 3D). This can be explained by the higher mechanical modulus and stiffness of the nucleus compared to the whole cells, which makes the nuclear deformation and conformity more difficult than cellular deformation.[62,63] The combination of the cell and nuclear deformation on micropatterns reveals a native shape of U2OS cells best matching a micropattern aspect ratio of 2.

Cell and Nuclear Shape Indices. To measure the cell shape index, we used the cell shape index (CSI) and nuclear shape index (NSI) (see the methods section). Specifically, for the CSI, classical image analysis was not sufficient to analyze the CSI due to the membrane protrusions, such as lamellipodia, on epithelial cells. Hence, we developed an automated cellular analysis based on the actin staining of the cells. We have optimized the smallest fitting convex hull that covers the shape to eradicate the effect of cellular irregularity (Figure 3E). Our analysis showed that CSI of cells complies with the protein-patterned shapes for various shapes. The average CSI values for the cells measured were 0.9, 0.76, 0.60, 0.69, 0.48, and 0.31 for the circle, square, triangle, rectangle 2, rectangle 5, and rectangle 10 shapes, respectively, showing minimal deviation from the protein patterned shape index (1, 0.79, 0.6, 0.7, 0.44, and 0.26 for the circle, square, triangle, rectangle 2, rectangle 5, and rectangle 10 shapes, respectively), as shown in Figure 3F. Our results also show that control nonpatterned cells exhibit a wide range of cell shapes on nanopillars (CSI range of ∼0.4−0.9) (Figure 3F,control). Therefore, our various engineered

https://doi.org/10.1021/acsnano.4c03743
ACS Nano 2024, 18, 19064−19076

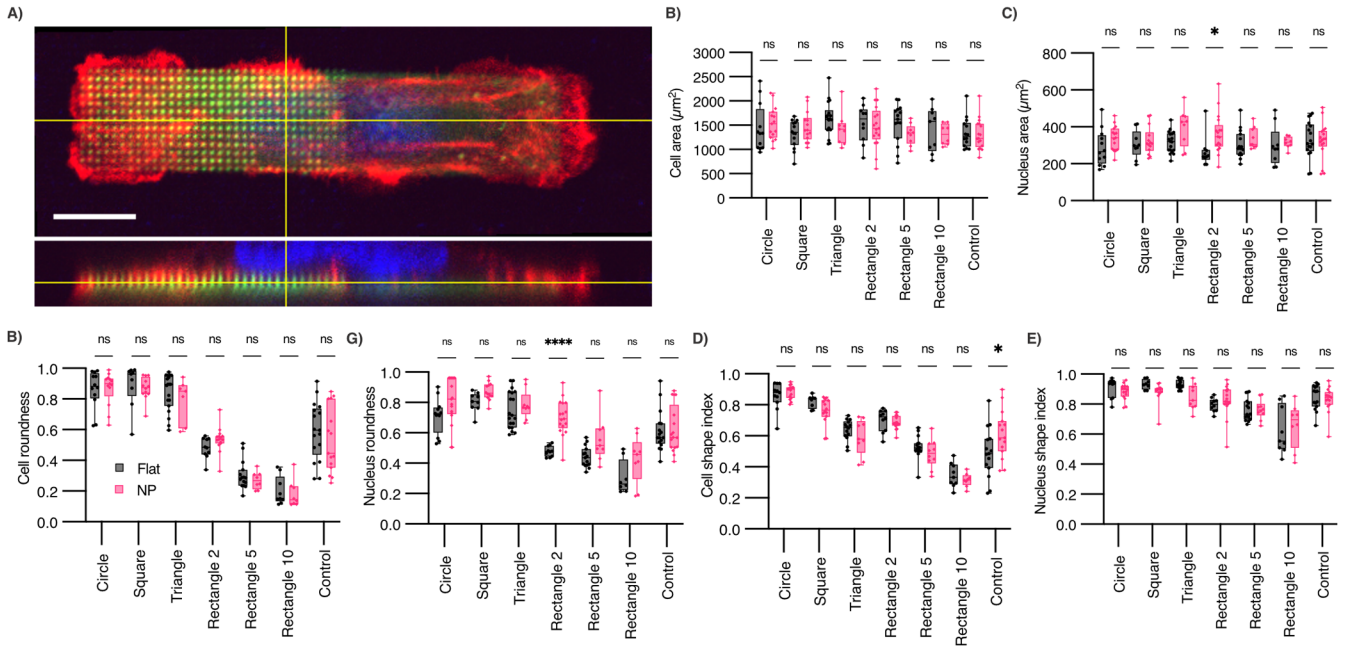

Figure 4. Comparison of morphologies of micropatterned cells on flat and nanopillar substrates. (A) Representative confocal top and side view images of a U2OS cell growing partially on flat and nanopillar area. ECM protein gelatin (green), actin (red), and nucleus (blue). Comparison of the (B) cell area and (C) nucleus area for cells growing on flat and nanopillar substrate. Comparison of the (D) cell and (E) nucleus roundness of the U2OS cells growing on flat and nanopillar substrate. (F) Cell and (G) nucleus shape index comparison of U2OS cells growing on flat and nanopillar substrates. (*p < 0.05, **p < 0.01, ***p < 0.001, and ****p < 0.0001).

micropattern shapes can precisely control the cell shape within the 0.4−0.9 control range (square, triangle, rectangle 2, and rectangle 5) or into new shapes that cells do not naturally adapt if not patterned (circle or rectangle 10). This is evident from the statistically significant difference between the CSI of nonpatterned control cells and cells on circle (P value of 0.001) and rectangle 10 (P value of 0.0001) micropatterns. Additionally, the difference in CSI of nonpatterned control cells was statistically insignificant from the CSI of cells on square, triangle, rectangle 2, and rectangle 5 micropatterns.

Interestingly, despite significant changes in cell shape on various micropattern shapes, the nuclear shape was only significantly different when comparing control nonpatterned cells, to highly elongated rectangle 10 patterns (NSI of 0.65 for rectangle 10 compared to NSI of 0.83 for nonpatterned) suggesting that the small width of the patterns impacts nuclear shape changes (Figure 3G). To demonstrate the controllability of the cellular shape on nanopillars using our technique, we compare the range of cell shapes on nanopillars with and without micropatterning. Our results shows that the micropatterning technique on nanopillars decreased the CSI range thoroughly across all geometries (Figure 3H).

Comparing Cellular Morphologies on Micropatterned Flat and Nanopillar Substrates. Moving from individual shape factors to analysis of cellular morphologies on flat and nanopillar substrates, we aimed to investigate the influence of the substrate topography on the cellular architecture. In the previous section, we demonstrated that cells can be confined to specific ECM shapes by comparing properties of cells on ECM-micropatterned and nonpatterned nanopillars. In this section, we have expanded our investigation into the changes in cell and nuclear morphology when cells were confined to micropatterns on nanopillars or flat substrates. The confocal image shown in Figure 4A of a cell confined partially to nanotopography and partially to a flat substrate provides a clear visual representation of the complex interplay between the cells and the substrate. By controlling cell shapes on both nanopillar and flat substrates, we were able to better determine how nanopillars affected cell and nuclear shape parameters and the coupling between the cell and nuclear shape in a confined 2D ECM. Comparing the cell area on flat and nanopillar surfaces, we found no notable differences, demonstrating that the controlled area of the cells on micropatterns was unaffected by the substrate shape (Figure 4B). Specifically, we observed that rectangular micropatterns with an aspect ratio of 2 manifested a difference in nuclear size between nanopillar and flat substrate, whereas the size was comparable on other micropattern shapes, implying that the nucleus itself possesses a degree of mechanosensitivity to the underlying topography (Figure 4C). This suggests a shape-dependent effect of nanopillar topography on nuclear morphology, justifying a more rigorous investigation into the relationship between cell shape and substrate influence.

We also compared the difference in cellular roundness between nanopillars and flat substrate (Figure 4D,E). While the effect of most shapes was independent of the nanotopography, rectangle 2 showed a significant difference for the nuclear roundness (p < 0.0001). These findings suggest that nanopillars may alter nuclear morphology only for particular cell shapes, which could be related to how the cytoskeletal elements involved in nuclear shape are organized on nanopillars for these cell shapes. Although we observed this phenomenon on rectangle 2, further studies would be required to determine how different cell types and nanopillar dimensions impact these results.[34,46] Additionally, results show that cells grown on nanopillars exhibit a higher shape index, indicative of a circular shape, consistent with previous

https://doi.org/10.1021/acsnano.4c03743
ACS Nano 2024, 18, 19064−19076

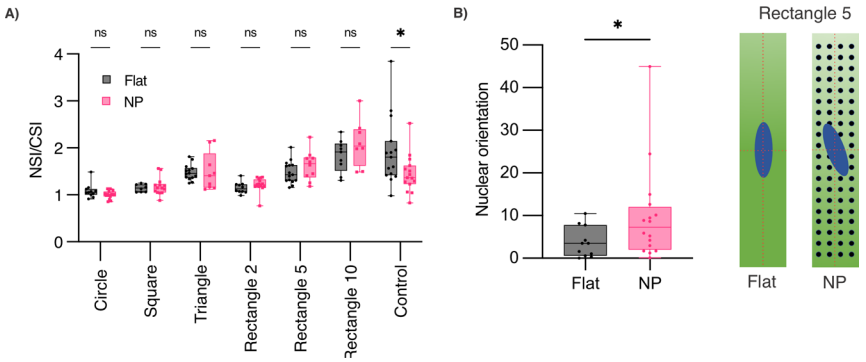

Figure 5. Effect of substrate and micropatterning on nuclear deformation and orientation for U2OS cells. (A) Comparison of nuclear shape index (NSI) to the cellular shape index (CSI) ratio on flat and nanopillar substrate. (B) Changes in nuclear orientation on rectangle 5 micropatterns on nanopillars compared with corresponding micropatterns on flat substrates. ($*p < 0.05$).

reports.[27] However, when micropatterned ECM was used to confine the cells, no statistically significant variation in cellular and nuclear control was observed between flat and nanopillar surfaces (Figure 4F,G). In light of these considerations, it is clear that the role of nanopillar topography in dictating cellular and nuclear morphology is both complex and shape-dependent.

Earlier studies of micropatterned cells on flat substrates have shown that the shape and orientation of the nucleus are coupled with that of the cell.[32] Hence, some studies have used cell micropatterning as a technique to control the shape of the nucleus.[64] We next determined whether nanopillars affect the coupling between cell shape and nuclear shape and orientation and whether we can control nuclear shape by micropatterning on nanopillars. To do this, we compared the ratio of NSI to CSI on nanopillars versus flat substrates. This ratio can be studied as an index to compare the relative deformation of the cell and nucleus, where a higher NSI-to-CSI ratio is indicative of more deformed cell, but less deformed nucleus.[32,65] Our results in Figure 5A show that there is a significant difference in NSI to CSI between cells cultured on flat substrates and nanopillars without micropatterning; however, when confining the cells with protein micropatterns, there is no significant difference between flat and nanopillar substrate suggesting that the nucleus can be deformed by controlling the cell shape on nanopillar substrates. However, our results show that the NSI-to-CSI ratio is highest for rectangle 10 suggesting that the nucleus is rounder and not deformed as much as the cell for this cell shape (Figure S6).[49−51] These results suggest that the nucleus can be controllably deformed by micropatterning and engineering cell morphology on nanopillars. However, the degree of nuclear deformation is limited for high aspect ratio cells.

We next asked whether nanopillars can affect the nuclear orientation on micropatterns when cells are elongated. Several studies have shown that cells and the nucleus reorient themselves along the direction of maximum stress to minimize the applied force. For example, cells on the elongated shapes align themselves along the major axis of the rectangle, which can cause the nucleus to be also aligned along the same axis.[32] We computed and compared the nuclear orientation on rectangle 5 between flat and nanopillar substrates. The flat substrate shows an absolute rotation of 3.7 ± 3.5° while the nanopillar shows 9.9 ± 11.2° values (Figure 5B). These findings suggests that nanopillars can disrupt the orientation and alignment of the nucleus that is caused by the cell shape. These findings and further studies using our technique can provide fundamental understanding of how nanopillars impact cell migration,[66] signaling,[67] and division.[68]

Effect of Cell Shape on Nanopillar-Enhanced Endocytosis and Transfection. Nanopillars are known to enhance cell endocytosis.[21] Previous studies have shown that especially nanoscale membrane curvature can enhance the clathrin-mediated endocytosis.[22,69] In order to further investigate the effect of nanopillars in combination with cellular elongation, we conducted experiments using U2OS cells and FM 1−43 dye[51] based on the previously described method.[21] FM 1−43 dye has minimal fluorescent signal when present in the solution; however, when it binds to the membrane, it will be highly fluorescent.[70]Figure 6A shows a schematic of the curvature-related enhancement of clathrin-mediated endocytosis and our results that nanopillars enhance the endocytosis compared to flat surface. Next, we studied the effects of elongation and cellular shape on nanopillar-enhanced endocytosis. Quantitative analysis of the endocytosis on nanopillars shows clearly that shapes with higher elongation (rectangular shapes) have more FM 1−43 dye endocytosis than circular shapes as shown in Figure 6B. Endocytosis is known to be regulated through the cytoskeleton, which has also been identified as the link between cell and nuclear shape regulation.[32] Since we observed that cells on rectangle 10 exhibited the least deformed nucleus (Figure 5B), this could indicate that the increased endocytosis is related to a disrupted cytoskeletal organization. Nanotopographies can likewise affect the cell cytoskeleton and endocytosis, which we believe highlights the importance of our platform for disentangling the effect of different topographical and biochemical cues.[6] This is extremely important due to the application of nanopillars for intracellular drug delivery and sensing platforms.[71]Figure 6C shows overlay images of U2OS cells on rectangular and circular shapes with the vesicles endocytosed to the cell. The results of these experiments provide insights into the complex nature of the cellular response to the substrate and cellular elongation.

We further investigated the influence of both cell morphology and substrate topography on the transfection efficiency. Cells growing on nanopillar structures exhibited a higher transfection efficiency compared to those on flat surfaces, suggesting that they may modulate cellular behavior to promote material uptake (Figure 6D,E). To study the effect of cell shape on the transfection efficiency on nanopillars, we micropatterned lines on the nanopillar to elongate cells (NP-

https://doi.org/10.1021/acsnano.4c03743
ACS Nano 2024, 18, 19064−19076

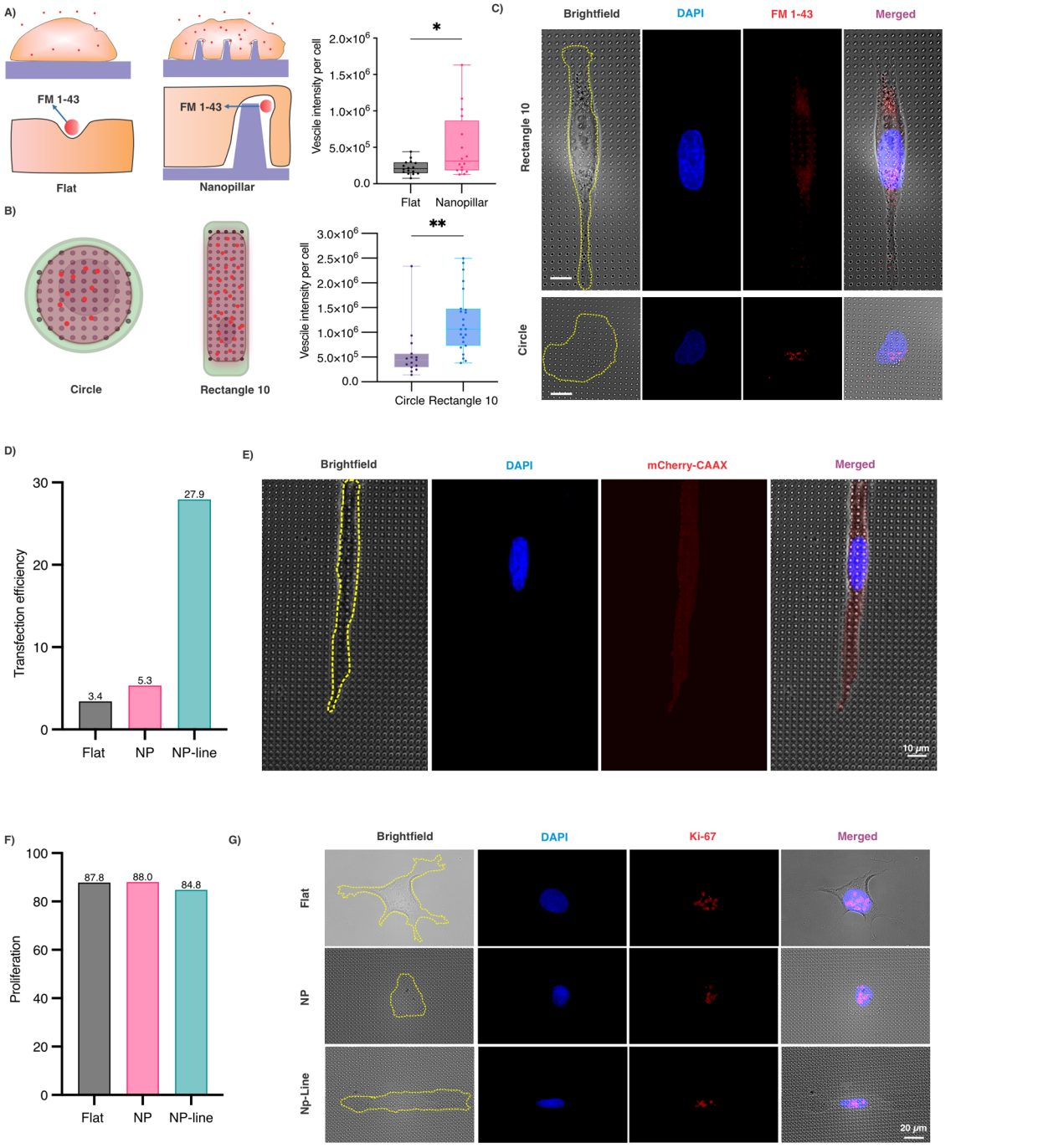

Figure 6. Endocytosis analysis of U2OS cells growing on different substrate and shapes. (A) Schematic showing the proposed mechanism of endocytosis based on substrate (flat and nanopillar) and quantitative analysis of endocytosed FM 1−43 dye in U2OS cells. (B) Schematic of U2OS cells growing in different geometries (circle and rectangle 10) on nanopillars and quantitative analysis of endocytosed FM 1−43 dye. (C) Representative fluorescence images of the FM 1−43 dye endocytosed in U2OS cells. Brightfield image is used to analyze cell shape, FM 1−43 dye (red) and nucleus (blue). (D) Quantitative analysis of transfection efficiency on different substrate and morphology fixed at 8 h upon transfection. (E) Representative fluorescent images of the cell transfected with mCherry-CAAX on NP-line. Brightfield used to visualized cell shape and nanopillars, mCherry-CAAX (red) and nucleus (blue). (F) Quantitative analysis of proliferation on different substrate and morphology. (G) Representative fluorescent images of the cell proliferation on different substrates (flat, NP, NP-line). Brightfield used to visualized cell shape, K_i-67 (red) and nucleus (blue). ($*p < 0.05$, and $**p < 0.01$).

line). We have used lines as our shape of interest to increase the throughput of the system compared to the specific shapes for stretching cells (rectangles 5 and rectangle 10). For this study, we have grown cells for 8 h on the nanopillars to allow complete attachment followed by transfection with an mCherry-CAAX construct for another 8 h. Cells were fixed at this point, intentionally before the standard transfection protocol's suggested duration, to focus our analysis on the dynamics of material uptake rather than the end-point efficiency. The improved efficiency of the NP-line can be attributed to the increased cell−surface interaction, which can facilitate a higher chance of plasmid uptake by the membrane.

https://doi.org/10.1021/acsnano.4c03743
ACS Nano 2024, 18, 19064−19076

This hypothesis is supported by our earlier findings that stretched cells on nanostructures can enhance clathrin-mediated endocytosis, providing a mechanistic basis for the observed uptake in efficiency. Additionally, the nanostructures and stretching can mimic in vivo environment, which can turn into a more favorable cellular response for transfection.

Furthermore, in our investigations into cell proliferation, we cultured cells on both nanopillar arrays with micropatterned lines and on uniformly coated surfaces. The data showed that while nanopillars slightly increased proliferation, the NP-lines led to a marginal decrease (Figure 6F,G). These findings suggest a negligible difference in proliferation rates across the surfaces, despite the significantly different topographies, which can be attributed to the cells' intrinsic ability to maintain proliferation despite minor alterations in the microenvironment. However, the modest reduction in proliferation on NP-line surfaces may be indicative of topography-induced alterations in cell behavior such as changes in cell cycle progression or differential activation of signaling pathways related to cell growth, which will require further investigations.

STUDY LIMITATION

Our study provides a multicue platform with the potential to control cell function and fate. However, this study faces some limitations that need to be further optimized. (1) This platform is limited to the adherent cells excluding applications for cells in suspension. (2) Determining the optimal cell density requires some optimization trials to capture single cells on micropatterns, which is challenging and requires optimization based on cell size. (3) Adhesion and spreading behaviors vary among different cell lines and even some heterogeneity within each cell line that requires optimization for complete cellular conformation to micropatterns. (4) The study of more complex environments, such as multicell culture or organoid platforms for a more realistic insight, is challenging to achieve with micropatterns. (5) Another practical limitation includes the difficulty for downstream analyses, like flow cytometry or RNA sequencing. (6) The scalability and throughput of this system need to be improved for further application of this system in delivery systems.

CONCLUSIONS

In this work, we presented a multicue platform that combines nanoscale topography with protein micropatterning to regulate cell behaviors through nanoscale membrane curvatures and controlled 2D cell geometry. Nanopillars are emerging as building blocks of platforms for a variety of exciting biomedical applications including fundamental electro- and mechanobiology,[16] cancer diagnostics,[72] and drug delivery and discovery.[11,12,73] Additionally, we have shown that maskless and contactless protein micropatterning can be used to modulate and regulate cellular shape and function on flat and nanopillar substrates. We demonstrated how our multicue platform can enhance nanotopography-mediated endocytosis by elongating cellular shapes on nanotopography. These findings have significant implications for the development of nanostructured platforms for biomolecule delivery. Furthermore, the precise control of cellular morphologies can add functionalities to biomaterials with nanotopography that are becoming more popular as building block of cell-based assays for applications such as malignancy detection,[72] probing cellular biophysics,[22,74] and cardiotoxicity screening.[16] For example, micropatterning of stem-cell-derived cardiac muscle cells onto nanopillar electrode platforms can not only improve maturation of these cells but also provide a more physiologically relevant environment for these cells. In addition, the control of cellular morphology and shape of various cell types on nanotopography, as illustrated in Figures 2 and 3, may significantly contribute to programming cells for applications in tissue engineering. Overall, this is a platform for creating a controlled microenvironment that enables the study of cellular functionality by investigating the effect of mechanical cues in a high-throughput manner.

EXPERIMENTAL METHODS

Nanopillar Fabrication. Nanopillar fabrication started with procurement of 4 in. fused quartz wafer from Wafer Pro (USA). The wafer underwent RCA cleaning using SC1 and SC3, followed by spin rinsing and drying in SRD (MEI). Subsequently, they were then spin-coated with an AZ 1512 photoresist (EMD Performance Materials Corp., USA) at 4000 rpm for 45 s at 12000 acc using a three-step process, resulting in a thickness of approximately 1.2 μm. The wafers were patterned and exposed (375 nm, dose 300) using our design file (.gds) in the Heidelberg MLA system. After exposure, the substrates were developed with an AZ400 (AZ Electronic Materials USA Corp) for 30 s and checked under an optical microscope. The Cr (99.998% target) metal was deposited onto the patterned substrate using a Temescal Ebeam evaporator, followed by a lift-off procedure using RR41, acetone, and IPA. The substrates were then dry etched for 50 min using the Oxford Plasmalab 80plus RIE system with Ar (35 sccm) and ChF3 (25 sccm) gases at 50 mT and 200 W to etch the wafer and create nanopillars. Finally, the substrates underwent wet etching for 10 min using Cr etchant (Transene Company Inc.) to remove the Cr, followed by BOE 20:1 for 16 min to remove the exposed quarts. The wafers were diced into 1 cm × 1 cm chips for further experiments.

Micropatterning Method. Maskless lithography method with PRIMO were done based on the described method[56] with modifications for patterning on a nanopillar surface. Briefly, nanopillar surface from quartz was UVO treated for 10 min to clean the surface and enhance the electrostatic adsorption of positively charged PLL (Sigma-Aldrich, USA) groups to the negatively charged surface. PLL solution (0.1 mg/L) was incubated on the surface for 30 min and washed with 0.1 M HEPES (Gibco, USA) buffer. Following PLL incubation, m-PEG-SVA (Laysan Bio, USA) with the concentration of 100 mg/mL was prepared and added to the surface and incubated for 1 h. The resulting PEG layer serves as an antifouling layer that can hinder protein and cellular attachment. The chips were washed 10 times with DI water and air-dried. The UV-sensitive PLPP gel (Alvéole, Fr) solution was mixed with 70% v/v ethanol and added to the dried surface and covered until micropatterning. The chips were mounted on a glass substrate on the stage of a Nikon Ti2 Eclipse microscope. The images were made by open-source software Inkscape and loaded into Leonardo (Alvéole, Fr) software. The patterns were projected using a 375 nm laser on an S Plan Fluor ELWD 20× with 0.45 NA objective with various doses. The projected area causes localized cleavage of the PEG-SVA, exposing PLL to the ECM protein attachment. Chips were washed with DI water 10 times and incubated with a 20 μg/mL mixture of FITC-gelatin (BioVision, USA) and FN (Sigma-Aldrich, USA) with a 1:1 w/w ratio. Chips were washed with 1× PBS (Gibco, USA) 10 times profusely to remove the extra protein and prepare the sample for cell seeding.

For the experiment testing the fate of PEG molecules during micropatterning, the m-PEG-SVA was replaced with FITC-PEG-SC (Biochempeg Scientific Inc., USA) and FITC-gelatin was replaced with Fibrinogen-A647 (Invitrogen, USA). The laser power was reduced to ensure a linear correlation between the theoretical dose and practical exposure.

SEM Imaging. Topography of the nanopillar arrays was characterized with scanning electron microscopy (Quanta FEG 250,

https://doi.org/10.1021/acsnano.4c03743
ACS Nano 2024, 18, 19064−19076

FEI), under low vacuum. Images were obtained at 5 kV with an Everhart Thornley detector (ETD). Images were taken under 45° tilted for height visualization.

Cell Culture and Seeding. U2OS(ATCC) cells were grown in McCoy's 5A Medium (ATCC) supplemented with 10% (v/v) fetal bovine serum (FBS) (Sigma-Aldrich, USA) and 1% (v/v) penicillin-streptomycin (Sigma-Aldrich, USA) and incubated at 37 °C with 5% CO2. U2OS cells at passages 2−8 were detached by TrypLE Express Enzyme (1×) (Gibco, USA). After centrifugation of the cell suspension, the supernatant was removed to achieve the cell pellet. Cell pellets were resuspended in the McCoy's 5a media and the abovementioned supplements. A 100 μL cell suspension with ∼1 × 10^4 was added to each nanopillar chips and incubated at 37 °C. Cells were washed after 30 min after initial adhesion to the ECM micropatterns to achieve single cells per patterns and media added the chip and incubated for growth. Cells were fixed after 24 h and used for further analysis.

Fluorescent Staining and Microscopy. After 24 h, cells were fixed with 4% paraformaldehyde (Electron Microscopy Sciences, USA) at room temperature for 10 min and washed with PBS. Cells were permeabilized with 1% with Triton X-100 (Sigma-Aldrich, USA) for 10 min and blocked in 2% (wt/vol) bovine serum albumin (BSA) (Thermo Scientific, USA) for 1 h. Samples were rinsed in PBS and incubated with 4′,6-diamidino-2-phenylindole (DAPI) (Thermo Scientific, USA) for 5 min and Alexa 594-phalloidin (Invitrogen, USA) for 20 min in dark for the nucleus and F-actin staining, respectively. For the proliferation study, cells were cultured on nanopillar and washed with PBS three times, fixed, and blocked as described earlier. A mouse anti-K_i-67 (Cell Signaling Technology, USA; dilution 1:1600) and antimouse-Alexa 598 (Invitrogen, USA; dilution 1:1000) secondary antibody were used to immunostained the cells. Images were collected with an Echo revolve microscope with 40× Plan Fluorite LWD CC with NA 0.60 and 60× PLAN Fluorite water dipping objective with NA 1.00.

Method for the Cell Analysis. The image analysis for the fluorescent images and morphology analysis were performed using ImageJ 1.53 (NIH, US). The signal intensity of the fluorescent labeled micropatterns was measured by selecting the shapes in grayscale and calculating the gray value of shapes after applying subtract background by choosing sliding paraboloid and enhancing contrast of the images by CLAHE by a block size of 19 and histogram bins of 256 with a maximum slope of 3. Additionally, the point-by-point signal of micropatterning was measured by using plot profile command as described elsewhere.[75] The area and roundness of cell and nucleus were calculated by analyze particle command as follows:

$$\text{roundness} = \frac{\text{minor axis}}{\text{major axis}} \tag{1}$$

The cellular shape index (CSI) was calculated based on actin staining to achieve the area and perimeters of the cell as follows.

$$\text{shape index} = \frac{4\pi \times \text{area}}{\text{perimeter}^2} \tag{2}$$

To remove the intensity dependency of analysis for the shape analysis, we have used the convexHull command of the OpenCV library using Python by drawing the smallest counters surrounding the cells to achieve more accurate values for cell and nucleus shape index (CSI and NSI) and rely solely on the shape of the objects.

To investigate the conformity of the cells to the micropatterned proteins as an indicator of micropatterning effectiveness, we have implemented Hu Moments for shape analysis of two objects. Hu Moments are a set of mathematical descriptors that can be used for shape analysis of objects while they are invariant to image transformations that allow Hu Moments to provide a reliable and consistent measurement of shape analysis. Raw image moment can be calculated using eq 1 while the $I(x, y)$ is the intensity of the pixel at given (x, y) location.[76]

$$M = \sum_x \sum_y I(x, y) \tag{3}$$

Endocytosis. For the endocytosis analysis, U2OS cells were cultured on various substrates after 24 h of incubation. Media was removed followed by washing the cells with PBS. FM 1−43 (ThermoFisher, USA) with 2 μM concentration was added to the well plate containing the nanopillar chip. Cells were incubated for 15 min with media containing FM 1−43 dye at 37 °C. Cells were washed with PBS and incubated for an additional 20 min at 37 °C. Cells were fixed with 4% PFA for 10 min and stained with 300 nM DAPI for 5 min. The samples were imaged and analyzed using ImageJ (NIH, USA) software.

Cell Transfection. U2OS cells were grown on the nanopillar chips for 8 h before transfection to ensure adhesion and spreading. The transfection was performed using ViaFect transfection reagent (Promega, USA) according to manufacturer's protocol. FusionRed-CAAX plasmid was cloned by fusing the DNA fragment encoding the CAAX motif of K-Ras protein (GKKKKKKSKTKCVIM) to the 3′ end of the linear pFusionRed-N vector (Evrogen, #FP412) via Gibson assembly.[77,78] For transfection, 500 ng of this plasmid was mixed with ViaFect reagents with a DNA:transfection reagent ratio of 1:3 and incubated at room temperature for 20 min. The complex was added to the cells on nanopillar chips containing growth medium and incubated in 37C for an additional 8 h.

Statistical Analysis. All the data are shown as the mean ± standard deviation (SD). Statistical significance with two-tailed Student's t test analysis with Welch's correction was performed in Prism (GraphPad, USA) to determine the statistical significance of the differences between the means of the different experimental groups. In addition, the results of Figure 4 for comparison of the cells on flat and nanopillar within different micropattern shapes were analyzed using two-way ANOVA, followed by Tukey's multiple comparisons post hoc analysis.

ASSOCIATED CONTENT

Supporting Information

The Supporting Information is available free of charge at https://pubs.acs.org/doi/10.1021/acsnano.4c03743.

Detailed visual and quantitative analyses complementing the main text; Figure S1 illustrates cell growth on different substrates, highlighting the differences in focal adhesion and curved adhesion on nanopillars; Figure S2 presents the dose optimization for light-induced protein patterning; Figure S3 showcases nanopillar micropatterning with various shapes, including profiles of protein intensity; Figure S4 compares micropatterning on nanopillars using different methods, demonstrating the effectiveness of light-induced protein patterning; Figure S5 offers immunofluorescent imaging of cells on flat versus nanopillar substrates, showing distinct morphological changes; Figure S6 displays the NSI-to-CSI ratios on micropatterned nanopillar substrates, indicating variations in cellular and nuclear deformation (PDF)

AUTHOR INFORMATION

Corresponding Authors

Lasse Hyldgaard Klausen − *Interdisciplinary Nanoscience Center (iNANO), Aarhus University, Aarhus C 8000, Denmark;* orcid.org/0000-0003-3004-5958; Email: lassehyldgaard@inano.au.dk

Zeinab Jahed − *Department of NanoEngineering and Department of Bioengineering, University of California San Diego, La Jolla, California 92093, United States;* orcid.org/0000-0002-0139-3219; Email: Zjahed@ucsd.edu

Authors

Einollah Sarikhani − *Department of NanoEngineering, University of California San Diego, La Jolla, California 92093, United States;* orcid.org/0000-0002-7841-5244

Dhivya Pushpa Meganathan − *Department of NanoEngineering, University of California San Diego, La Jolla, California 92093, United States*

Anne-Kathrine Kure Larsen − *Interdisciplinary Nanoscience Center (iNANO), Aarhus University, Aarhus C 8000, Denmark*

Keivan Rahmani − *Department of NanoEngineering, University of California San Diego, La Jolla, California 92093, United States*

Ching-Ting Tsai − *Department of Chemistry, Stanford University, Stanford, California 94305, United States*

Chih-Hao Lu − *Department of Chemistry, Stanford University, Stanford, California 94305, United States*

Abel Marquez-Serrano − *Department of NanoEngineering, University of California San Diego, La Jolla, California 92093, United States*

Leah Sadr − *Department of NanoEngineering, University of California San Diego, La Jolla, California 92093, United States*

Xiao Li − *Department of Chemistry, Stanford University, Stanford, California 94305, United States;* orcid.org/0000-0002-1200-8590

Mingdong Dong − *Interdisciplinary Nanoscience Center (iNANO), Aarhus University, Aarhus C 8000, Denmark;* orcid.org/0000-0002-2025-2171

Francesca Santoro − *Center for Advanced Biomaterials for Healthcare, Tissue Electronics, Instituto Italiano di Tecnologia, Naples 80125, Italy; Faculty of Electrical Engineering and IT, RWTH, Aachen 52074, Germany; Institute for Biological Information Processing-Bioelectronics, Forschungszentrum Juelich, Julich 52428, Germany;* orcid.org/0000-0001-7323-9504

Bianxiao Cui − *Department of Chemistry, Stanford University, Stanford, California 94305, United States;* orcid.org/0000-0002-8044-5629

Complete contact information is available at: https://pubs.acs.org/10.1021/acsnano.4c03743

Notes

The authors declare no competing financial interest.

This work was previously submitted to a preprint server and can be cited as Sarikhani, E.; Meganathan, D. P.; Rahmani, K.; Tsai, C.-T.; Marquez-Serrano, A.; Li, X.; Santoro, F.; Cui, B.; Klausen, L. H.; Jahed, Z. Engineering Cell and Nuclear Morphology on Nano Topography by Contact-Free Protein Micropatterning. 2023, Article Number: 2023.06.05.543791. bioRxiv. URL: 10.1101/2023.06.05.543791 (accessed June 7, 2023).

ACKNOWLEDGMENTS

This work was performed in part at the San Diego Nanotechnology Infrastructure (SDNI) of UCSD, a member of the National Nanotechnology Coordinated Infrastructure, which is supported by the National Science Foundation (Grant ECCS-2025752). We would like to thank Dr. Peng Guo and the Nikon Imaging Center at UCSD for the support on microscopy experiments. This work was in part supported by Air Force Office of Scientific Research YIP award (award number: 311616-00001) and Cancer research coordinating committee faculty seed grant to Z.J. We acknowledge support from the Independent Research Fund Denmark (9040-00219B), the Carlsberg Foundation (CF19-0742), VILLUM FONDEN (project 50411), and the European Union's Horizon Europe programme under Marie Skłodowska-Curie Actions − Staff Exchanges (SE) grant agreement no. 101086226-ENSIGN. Additionally, we acknowledge the Stanford University Center for Molecular Analysis and Design (CMAD) fellowship for C.-H.L. We thank the developers of the open-source software Inkscape, which was used to create the images for micropatterning.

REFERENCES

(1) Gaharwar, A. K.; Singh, I.; Khademhosseini, A. Engineered Biomaterials for in Situ Tissue Regeneration. *Nat. Rev. Mater.* **2020**, *5* (9), 686−705.

(2) Hussey, G. S.; Dziki, J. L.; Badylak, S. F. Extracellular Matrix-Based Materials for Regenerative Medicine. *Nat. Rev. Mater.* **2018**, *3* (7), 159−173.

(3) Liu, Z.; Tang, M.; Zhao, J.; Chai, R.; Kang, J. Looking into the Future: Toward Advanced 3D Biomaterials for Stem-Cell-Based Regenerative Medicine. *Adv. Mater.* **2018**, *30* (17), 1705388.

(4) Bashor, C. J.; Hilton, I. B.; Bandukwala, H.; Smith, D. M.; Veiseh, O. Engineering the next Generation of Cell-Based Therapeutics. *Nat. Rev. Drug Discov* **2022**, *21* (9), 655−675.

(5) Shao, Y.; Fu, J. Integrated Micro/Nanoengineered Functional Biomaterials for Cell Mechanics and Mechanobiology: A Materials Perspective. *Adv. Mater.* **2014**, *26* (10), 1494−1533.

(6) Lou, H.-Y.; Zhao, W.; Zeng, Y.; Cui, B. The Role of Membrane Curvature in Nanoscale Topography-Induced Intracellular Signaling. *Acc. Chem. Res.* **2018**, *51* (5), 1046−1053.

(7) Milos, F.; Belu, A.; Mayer, D.; Maybeck, V.; Offenhäusser, A. Polymer Nanopillars Induce Increased Paxillin Adhesion Assembly and Promote Axon Growth in Primary Cortical Neurons. *Adv. Biol.* **2021**, *5* (2), 2000248.

(8) Sorgato, M.; Guidi, E.; Conconi, M. T.; Lucchetta, G. Surface Nanostructuring of Bioresorbable Implants to Induce Osteogenic Differentiation of Human Mesenchymal Stromal Cells. *CIRP Annals* **2021**, *70* (1), 463−466.

(9) Das Ghosh, L.; Hasan, J.; Jain, A.; Sundaresan, N. R.; Chatterjee, K. A Nanopillar Array on Black Titanium Prepared by Reactive Ion Etching Augments Cardiomyogenic Commitment of Stem Cells. *Nanoscale* **2019**, *11* (43), 20766−20776.

(10) He, G.; Chen, H.-J.; Liu, D.; Feng, Y.; Yang, C.; Hang, T.; Wu, J.; Cao, Y.; Xie, X. Fabrication of Various Structures of Nanostraw Arrays and Their Applications in Gene Delivery. *Adv. Mater. Interfaces* **2018**, *5* (10), 1701535.

(11) Stewart, M. P.; Sharei, A.; Ding, X.; Sahay, G.; Langer, R.; Jensen, K. F. In Vitro and Ex Vivo Strategies for Intracellular Delivery. *Nature* **2016**, *538* (7624), 183−192.

(12) Ma, Y.; Nolte, R. J. M.; Cornelissen, J. J. L. M. Virus-Based Nanocarriers for Drug Delivery. *Adv. Drug Deliv Rev.* **2012**, *64* (9), 811−825.

(13) Lee, W. S.; Ahn, J.; Jung, S.; Lee, J.; Kang, T.; Jeong, J. Biomimetic Nanopillar-Based Biosensor for Label-Free Detection of Influenza A Virus. *Biochip J.* **2021**, *15* (3), 260−267.

(14) Cui, S.; Tian, C.; Mao, J.; Wu, W.; Fu, Y. Nanopillar Array-Based Plasmonic Metasurface for Switchable Multifunctional Biosensing. *Opt. Commun.* **2022**, *506*, No. 127548.

(15) Losero, E.; Jagannath, S.; Pezzoli, M.; Lashuel, H. A.; Galland, C.; Quack, N. Neuronal Growth on High-Aspect-Ratio Diamond Nanopillar Arrays for Biosensing Applications. *Sci. Rep.* **2023**, *13*, 5909.

(16) Jahed, Z.; Yang, Y.; Tsai, C.-T.; Foster, E. P.; McGuire, A. F.; Yang, H.; Liu, A.; Forro, C.; Yan, Z.; Jiang, X.; Zhao, M.-T.; Zhang, W.; Li, X.; Li, T.; Pawlosky, A.; Wu, J. C.; Cui, B. Nanocrown

Electrodes for Parallel and Robust Intracellular Recording of Cardiomyocytes. *Nat. Commun.* **2022**, *13* (1), 2253.
(17) Zhang, W.; Lu, C.-H.; Nakamoto, M. L.; Tsai, C.-T.; Roy, A. R.; Lee, C. E.; Yang, Y.; Jahed, Z.; Li, X.; Cui, B. Curved Adhesions Mediate Cell Attachment to Soft Matrix Fibres in Three Dimensions. *Nat. Cell Biol.* **2023**, *25* (10), 1453−1464.
(18) Jahed, Z.; Molladavoodi, S.; Seo, B. B.; Gorbet, M.; Tsui, T. Y.; Mofrad, M. R. K. Cell Responses to Metallic Nanostructure Arrays with Complex Geometries. *Biomaterials* **2014**, *35* (34), 9363−9371.
(19) Lu, C.-H.; Tsai, C.-T.; Jones, T., IV; Chim, V.; Klausen, L. H.; Zhang, W.; Li, X.; Jahed, Z.; Cui, B. A NanoCurvS Platform for Quantitative and Multiplex Analysis of Curvature-Sensing Proteins. *Biomater. Sci.* **2023**, *11* (15), 5205−5217.
(20) Li, X.; Matino, L.; Zhang, W.; Klausen, L.; McGuire, A. F.; Lubrano, C.; Zhao, W.; Santoro, F.; Cui, B. A Nanostructure Platform for Live-Cell Manipulation of Membrane Curvature. *Nat. Protoc* **2019**, *14* (6), 1772−1802.
(21) Li, X.; Klausen, L. H.; Zhang, W.; Jahed, Z.; Tsai, C.-T.; Li, T. L.; Cui, B. Nanoscale Surface Topography Reduces Focal Adhesions and Cell Stiffness by Enhancing Integrin Endocytosis. *Nano Lett.* **2021**, *21* (19), 8518−8526.
(22) Zhao, W.; Hanson, L.; Lou, H.-Y.; Akamatsu, M.; Chowdary, P. D.; Santoro, F.; Marks, J. R.; Grassart, A.; Drubin, D. G.; Cui, Y.; Cui, B. Nanoscale Manipulation of Membrane Curvature for Probing Endocytosis in Live Cells. *Nat. Nanotechnol* **2017**, *12* (8), 750−756.
(23) Teo, B. K. K.; Goh, S.-H.; Kustandi, T. S.; Loh, W. W.; Low, H. Y.; Yim, E. K. F. The Effect of Micro and Nanotopography on Endocytosis in Drug and Gene Delivery Systems. *Biomaterials* **2011**, *32* (36), 9866−9875.
(24) Zhou, J.; Zhang, X.; Sun, J.; Dang, Z.; Li, J.; Li, X.; Chen, T. The Effects of Surface Topography of Nanostructure Arrays on Cell Adhesion. *Phys. Chem. Chem. Phys.* **2018**, *20* (35), 22946−22951.
(25) Beckwith, K. S.; Ullmann, S.; Vinje, J.; Sikorski, P. Influence of Nanopillar Arrays on Fibroblast Motility, Adhesion, and Migration Mechanisms. *Small* **2019**, *15* (43), 1902514.
(26) Wang, K.; Man, K.; Liu, J.; Meckes, B.; Yang, Y. Dissecting Physical and Biochemical Effects in Nanotopographical Regulation of Cell Behavior. *ACS Nano* **2023**, *17* (3), 2124−2133.
(27) Modaresifar, K.; Ganjian, M.; Díaz-Payno, P. J.; Klimopoulou, M.; Koedam, M.; van der Eerden, B. C. J.; Fratila-Apachitei, L. E.; Zadpoor, A. A. Mechanotransduction in High Aspect Ratio Nanostructured Meta-Biomaterials: The Role of Cell Adhesion, Contractility, and Transcriptional Factors. *Mater. Today Bio* **2022**, *16*, No. 100448.
(28) Lestrell, E.; Chen, Y.; Aslanoglou, S.; O'Brien, C. M.; Elnathan, R.; Voelcker, N. H. Silicon Nanoneedle-Induced Nuclear Deformation: Implications for Human Somatic and Stem Cell Nuclear Mechanics. *ACS Appl. Mater. Interfaces* **2022**, *14* (40), 45124−45136.
(29) Yang, L.; Jurczak, K. M.; Ge, L.; van Rijn, P. High-Throughput Screening and Hierarchical Topography-Mediated Neural Differentiation of Mesenchymal Stem Cells. *Adv. Healthcare Mater.* **2020**, *9* (11), 2000117.
(30) Li, N.; Jin, K.; Chen, T.; Li, X. A Static Force Model to Analyze the Nuclear Deformation on Cell Adhesion to Vertical Nanostructures. *Soft Matter* **2022**, *18* (35), 6638−6644.
(31) Capozza, R.; Caprettini, V.; Gonano, C. A.; Bosca, A.; Moia, F.; Santoro, F.; De Angelis, F. Cell Membrane Disruption by Vertical Micro-/Nanopillars: Role of Membrane Bending and Traction Forces. *ACS Appl. Mater. Interfaces* **2018**, *10* (34), 29107−29114.
(32) Versaevel, M.; Grevesse, T.; Gabriele, S. Spatial Coordination between Cell and Nuclear Shape within Micropatterned Endothelial Cells. *Nat. Commun.* **2012**, *3* (1), 671.
(33) Elnathan, R.; Tay, A.; Voelcker, N. H.; Chiappini, C. The Start-Ups Taking Nanoneedles into the Clinic. *Nat. Nanotechnol.* **2022**, *17*, 807.
(34) Hanson, L.; Zhao, W.; Lou, H.-Y.; Lin, Z. C.; Lee, S. W.; Chowdary, P.; Cui, Y.; Cui, B. Vertical Nanopillars for in Situ Probing of Nuclear Mechanics in Adherent Cells. *Nat. Nanotechnol* **2015**, *10* (6), 554−562.
(35) von Erlach, T. C.; Bertazzo, S.; Wozniak, M. A.; Horejs, C.-M.; Maynard, S. A.; Attwood, S.; Robinson, B. K.; Autefage, H.; Kallepitis, C.; del Río Hernández, A.; Chen, C. S.; Goldoni, S.; Stevens, M. M. Cell-Geometry-Dependent Changes in Plasma Membrane Order Direct Stem Cell Signalling and Fate. *Nat. Mater.* **2018**, *17* (3), 237−242.
(36) Hanson, L.; Lin, Z. C.; Xie, C.; Cui, Y.; Cui, B. Characterization of the Cell−Nanopillar Interface by Transmission Electron Microscopy. *Nano Lett.* **2012**, *12* (11), 5815−5820.
(37) Nakamoto, M. L.; Forró, C.; Zhang, W.; Tsai, C.-T.; Cui, B. Expansion Microscopy for Imaging the Cell−Material Interface. *ACS Nano* **2022**, *16* (5), 7559−7571.
(38) D'Arcangelo, E.; McGuigan, A. P. Micropatterning Strategies to Engineer Controlled Cell and Tissue Architecture in Vitro. *Biotechniques* **2015**, *58* (1), 13−23.
(39) Zhang, J.; Luo, Y.; Poh, C. L. Blue Light-Directed Cell Migration, Aggregation, and Patterning. *J. Mol. Biol.* **2020**, *432* (10), 3137−3148.
(40) Muzzio, N. E.; Horowitz, C. M.; Azzaroni, O.; Moya, S. E.; Pasquale, M. A. Tilted Mammalian Cell Colony Propagation Dynamics on Patterned Substrates. *Chaos Solitons Fractals* **2021**, *146*, No. 110841.
(41) Hou, Y.; Xie, W.; Achazi, K.; Cuellar-Camacho, J. L.; Melzig, M. F.; Chen, W.; Haag, R. Injectable Degradable PVA Microgels Prepared by Microfluidic Technology for Controlled Osteogenic Differentiation of Mesenchymal Stem Cells. *Acta Biomater* **2018**, *77*, 28−37.
(42) Théry, M.; Bornens, M. Cell Shape and Cell Division. *Curr. Opin Cell Biol.* **2006**, *18* (6), 648−657.
(43) McBeath, R.; Pirone, D. M.; Nelson, C. M.; Bhadriraju, K.; Chen, C. S. Cell Shape, Cytoskeletal Tension, and RhoA Regulate Stem Cell Lineage Commitment. *Dev Cell* **2004**, *6* (4), 483−495.
(44) Kilian, K. A.; Bugarija, B.; Lahn, B. T.; Mrksich, M. Geometric Cues for Directing the Differentiation of Mesenchymal Stem Cells. *Proc. Natl. Acad. Sci. U. S. A.* **2010**, *107* (11), 4872−4877.
(45) Batalov, I.; Jallerat, Q.; Kim, S.; Bliley, J.; Feinberg, A. W. Engineering Aligned Human Cardiac Muscle Using Developmentally Inspired Fibronectin Micropatterns. *Sci. Rep* **2021**, *11* (1), 11502.
(46) Wang, X.; Hu, X.; Kawazoe, N.; Yang, Y.; Chen, G. Manipulating Cell Nanomechanics Using Micropatterns. *Adv. Funct Mater.* **2016**, *26* (42), 7634−7643.
(47) Kim, M.-H.; Sawada, Y.; Taya, M.; Kino-oka, M. Influence of Surface Topography on the Human Epithelial Cell Response to Micropatterned Substrates with Convex and Concave Architectures. *J. Biol. Eng.* **2014**, *8* (1), 13.
(48) Bosch-Fortea, M.; Rodriguez-Fraticelli, A. E.; Herranz, G.; Hachimi, M.; Barea, M. D.; Young, J.; Ladoux, B.; Martin-Belmonte, F. Micropattern-Based Platform as a Physiologically Relevant Model to Study Epithelial Morphogenesis and Nephrotoxicity. *Biomaterials* **2019**, *218*, No. 119339.
(49) Xie, C.; Lin, Z.; Hanson, L.; Cui, Y.; Cui, B. Intracellular Recording of Action Potentials by Nanopillar Electroporation. *Nat. Nanotechnol* **2012**, *7* (3), 185−190.
(50) Abbott, J.; Ye, T.; Krenek, K.; Gertner, R. S.; Ban, S.; Kim, Y.; Qin, L.; Wu, W.; Park, H.; Ham, D. A Nanoelectrode Array for Obtaining Intracellular Recordings from Thousands of Connected Neurons. *Nat. Biomed Eng.* **2020**, *4* (2), 232−241.
(51) Hardelauf, H.; Waide, S.; Sisnaiske, J.; Jacob, P.; Hausherr, V.; Schöbel, N.; Janasek, D.; van Thriel, C.; West, J. Micropatterning Neuronal Networks. *Analyst* **2014**, *139* (13), 3256−3264.
(52) Czöndör, K.; Garcia, M.; Argento, A.; Constals, A.; Breillat, C.; Tessier, B.; Thoumine, O. Micropatterned Substrates Coated with Neuronal Adhesion Molecules for High-Content Study of Synapse Formation. *Nat. Commun.* **2013**, *4* (1), 2252.
(53) Hong, N.; Nam, Y. Thermoplasmonic Neural Chip Platform for in Situ Manipulation of Neuronal Connections in Vitro. *Nat. Commun.* **2020**, *11* (1), 6313.
(54) Seong, H.; Higgins, S. G.; Penders, J.; Armstrong, J. P. K.; Crowder, S. W.; Moore, A. C.; Sero, J. E.; Becce, M.; Stevens, M. M.

https://doi.org/10.1021/acsnano.4c03743
ACS Nano 2024, 18, 19064−19076

Size-Tunable Nanoneedle Arrays for Influencing Stem Cell Morphology, Gene Expression, and Nuclear Membrane Curvature. *ACS Nano* **2020**, *14* (5), 5371−5381.
(55) Bucaro, M. A.; Vasquez, Y.; Hatton, B. D.; Aizenberg, J. Fine-Tuning the Degree of Stem Cell Polarization and Alignment on Ordered Arrays of High-Aspect-Ratio Nanopillars. *ACS Nano* **2012**, *6* (7), 6222−6230.
(56) Strale, P.-O.; Azioune, A.; Bugnicourt, G.; Lecomte, Y.; Chahid, M.; Studer, V. Multiprotein Printing by Light-Induced Molecular Adsorption. *Adv. Mater.* **2016**, *28* (10), 2024−2029.
(57) Melero, C.; Kolmogorova, A.; Atherton, P.; Derby, B.; Reid, A.; Jansen, K.; Ballestrem, C. Light-Induced Molecular Adsorption of Proteins Using the PRIMO System for Micro-Patterning to Study Cell Responses to Extracellular Matrix Proteins. *JoVE* **2019**, *152*, No. e60092.
(58) Toro-Nahuelpan, M.; Zagoriy, I.; Senger, F.; Blanchoin, L.; Théry, M.; Mahamid, J. Tailoring Cryo-Electron Microscopy Grids by Photo-Micropatterning for in-Cell Structural Studies. *Nat. Methods* **2020**, *17* (1), 50−54.
(59) Žunić, D.; Žunić, J. Shape Ellipticity Based on the First Hu Moment Invariant. *Inf Process Lett.* **2013**, *113* (19−21), 807−810.
(60) Aubin, H.; Nichol, J. W.; Hutson, C. B.; Bae, H.; Sieminski, A. L.; Cropek, D. M.; Akhyari, P.; Khademhosseini, A. Directed 3D Cell Alignment and Elongation in Microengineered Hydrogels. *Biomaterials* **2010**, *31* (27), 6941−6951.
(61) Kim, D.-H.; Lipke, E. A.; Kim, P.; Cheong, R.; Thompson, S.; Delannoy, M.; Suh, K.-Y.; Tung, L.; Levchenko, A. Nanoscale Cues Regulate the Structure and Function of Macroscopic Cardiac Tissue Constructs. *Proc. Natl. Acad. Sci. U. S. A.* **2010**, *107* (2), 565−570.
(62) Zhang, J.; Alisafaei, F.; Nikolić, M.; Nou, X. A.; Kim, H.; Shenoy, V. B.; Scarcelli, G. Nuclear Mechanics within Intact Cells Is Regulated by Cytoskeletal Network and Internal Nanostructures. *Small* **2020**, *16* (18), 1907688.
(63) Barreto, S.; Clausen, C. H.; Perrault, C. M.; Fletcher, D. A.; Lacroix, D. A Multi-Structural Single Cell Model of Force-Induced Interactions of Cytoskeletal Components. *Biomaterials* **2013**, *34* (26), 6119−6126.
(64) Bautista, M.; Fernandez, A.; Pinaud, F. A Micropatterning Strategy to Study Nuclear Mechanotransduction in Cells. *Micromachines (Basel)* **2019**, *10* (12), 810.
(65) Liu, R.; Liu, Q.; Pan, Z.; Liu, X.; Ding, J. Cell Type and Nuclear Size Dependence of the Nuclear Deformation of Cells on a Micropillar Array. *Langmuir* **2019**, *35* (23), 7469−7477.
(66) Maninová, M.; Iwanicki, M. P.; Vomastek, T. Emerging Role for Nuclear Rotation and Orientation in Cell Migration. *Cell Adh Migr* **2014**, *8* (1), 42−48.
(67) Gundersen, G. G.; Worman, H. J. Nuclear Positioning. *Cell* **2013**, *152* (6), 1376−1389.
(68) Gudipaty, S. A.; Lindblom, J.; Loftus, P. D.; Redd, M. J.; Edes, K.; Davey, C. F.; Krishnegowda, V.; Rosenblatt, J. Mechanical Stretch Triggers Rapid Epithelial Cell Division through Piezo1. *Nature* **2017**, *543* (7643), 118−121.
(69) Akamatsu, M.; Vasan, R.; Serwas, D.; Ferrin, M. A.; Rangamani, P.; Drubin, D. G. Principles of Self-Organization and Load Adaptation by the Actin Cytoskeleton during Clathrin-Mediated Endocytosis. *Elife* **2020**, *9*, No. e49840.
(70) Bertrand, C. A.; Laboisse, C.; Hopfer, U.; Bridges, R. J.; Frizzell, R. A. Methods for Detecting Internalized, FM 1−43 Stained Particles in Epithelial Cells and Monolayers. *Biophys. J.* **2006**, *91* (10), 3872−3883.
(71) Chen, N.; He, Y.; Zang, M.; Zhang, Y.; Lu, H.; Zhao, Q.; Wang, S.; Gao, Y. Approaches and Materials for Endocytosis-Independent Intracellular Delivery of Proteins. *Biomaterials* **2022**, *286*, No. 121567.
(72) Zeng, Y.; Zhuang, Y.; Vinod, B.; Guo, X.; Mitra, A.; Chen, P.; Saggio, I.; Shivashankar, G. V.; Gao, W.; Zhao, W. Guiding Irregular Nuclear Morphology on Nanopillar Arrays for Malignancy Differentiation in Tumor Cells. *Nano Lett.* **2022**, *22* (18), 7724−7733.
(73) Xie, X.; Xu, A. M.; Leal-Ortiz, S.; Cao, Y.; Garner, C. C.; Melosh, N. A. Nanostraw−Electroporation System for Highly Efficient Intracellular Delivery and Transfection. *ACS Nano* **2013**, *7* (5), 4351−4358.
(74) Lou, H.-Y.; Zhao, W.; Li, X.; Duan, L.; Powers, A.; Akamatsu, M.; Santoro, F.; McGuire, A. F.; Cui, Y.; Drubin, D. G.; Cui, B. Membrane Curvature Underlies Actin Reorganization in Response to Nanoscale Surface Topography. *Proc. Natl. Acad. Sci. U. S. A.* **2019**, *116* (46), 23143−23151.
(75) Horzum, U.; Ozdil, B.; Pesen-Okvur, D. Step-by-Step Quantitative Analysis of Focal Adhesions. *MethodsX* **2014**, *1*, 56−59.
(76) Körtgen, M.; Park, G.-J.; Novotni, M.; Klein, R.3D Shape Matching with 3D Shape Contexts. In *The 7th Central European Seminar on Computer Graphics*; Budmerice Slovakia, 2003; Vol. *3*, pp 5−17.
(77) Lu, C.-H.; Pedram, K.; Tsai, C.-T.; Jones, T.; Li, X.; Nakamoto, M. L.; Bertozzi, C. R.; Cui, B. Membrane Curvature Regulates the Spatial Distribution of Bulky Glycoproteins. *Nat. Commun.* **2022**, *13* (1), 3093.
(78) Wright, L. P.; Philips, M. R. Thematic Review Series: Lipid Posttranslational Modifications CAAX Modification and Membrane Targeting of Ras. *J. Lipid Res.* **2006**, *47* (5), 883−891.

https://doi.org/10.1021/acsnano.4c03743
ACS Nano 2024, 18, 19064−19076